



# Study on an artificial phenomenon observed in terahertz biological imaging

ZHONGBO YANG,<sup>1,2,5</sup>  MUYANG ZHANG,<sup>3,5</sup> DANDAN LI,<sup>1</sup> LIGANG CHEN,<sup>1</sup> AILING FU,<sup>4</sup> YANMEI LIANG,<sup>3,6</sup>  AND HUABIN WANG<sup>1,2,7</sup>

<sup>1</sup>Center for Applied Physics and Chongqing Engineering Research Center of High-Resolution and Three-Dimensional Dynamic Imaging Technology, Chongqing Institute of Green and Intelligent Technology, Chinese Academy of Sciences, Chongqing 400714, China

<sup>2</sup>Chongqing School, University of Chinese Academy of Sciences, Chongqing 400714, China

<sup>3</sup>Institute of Modern Optics, Nankai University, Tianjin 300350, China

<sup>4</sup>School of Pharmaceutical Sciences, Southwest University, Chongqing 400716, China

<sup>5</sup>These authors contributed equally to this work

<sup>6</sup>ymliang@nankai.edu.cn

<sup>7</sup>wanghuabin@cigit.ac.cn

**Abstract:** Terahertz (THz) wave-based imaging of biological samples is an emerging but promising field. In the present work, we report an artificial phenomenon observed in imaging melanoma slices, which can lead to mistakenly interpretation of the experimental results. It was observed that a structure similar to but smaller than the sample contour appeared inside the melanoma slice image. The underlying mechanism of this phenomenon was then investigated both experimentally and theoretically. By imaging a regular standard sample (vinyl coverslip) with a THz time domain spectroscopy (THz-TDS) system and reconstructing its images at 0.8 and 1.2 THz, we can clearly observe the afore-mentioned artifacts. The experimental results are highly consistent with the simulations based on the Fresnel-Kirchhoff diffraction theory in which possible optical aberrations were incorporated. It can be concluded that this artifact was caused by the frequency-dependent diffraction of the sample edge. The work demonstrated here is essential for correct interpretation of the images obtained by the THz-TDS technique.

© 2021 Optical Society of America under the terms of the [OSA Open Access Publishing Agreement](#)

## 1. Introduction

Terahertz (THz) radiation normally refers to the electromagnetic wave with a frequency ranging from 0.1 to 10 THz (1 THz =  $10^{12}$  Hz). Due the unique photoelectronic properties of THz wave, THz-based imaging techniques can be employed to characterize various materials nondestructively and conveniently, and can provide rich structural, physical and chemical information of the samples that cannot be easily accessed by other imaging techniques [1–5]. Particularly, THz time domain spectroscopy (THz-TDS) imaging techniques have been recognized as useful tools for biological studies in recent years for their safe, label-free and chemical fingerprint properties, and they are attracting intense interest among the scientific communities [6–11]. For examples, Song et al. successfully assessed the water content of plant leaves with the transmission mode THz-TDS imaging technique [12], and Yamaguchi et al. achieved the image of rat melanoma tissues with the reflection mode THz-TDS imaging technique [13].

Generally, THz imaging techniques are still in the developing stage, and they are relatively new when compared to many conventional optical imaging techniques such as infrared imaging and visible light imaging techniques [14]. Hitherto, our knowledge on THz imaging is very limited, and unusual phenomena may be observed in THz imaging experiments. Consequently, it is an important task to explore the underlying mechanisms of unusual phenomena encountered in THz imaging, which is a crucial step for the proper interpretation of experimental data, and the development and application of THz imaging techniques.

Recently, we imaged mouse melanoma slices with a commercial THz-TDS system, and found an artifact appeared on the THz images of the samples, i.e., a structure resembling to the sample contour presented in the images. Based on our knowledge, this phenomenon has not been reported previously. Since this phenomenon can mislead the data interpretation, it is essential to investigate and clarify the underlying mechanisms of this phenomenon.

To this end, we interrogated the underlying physical mechanisms of the observed phenomenon in the present work, both experimentally and theoretically. In the experiment, we imaged a uniform vinyl coverslip with the THz-TDS system and analyzed its THz images at 0.8 and 1.2 THz. The artifact can be clearly observed in the images, which is highly similar to that observed on the melanoma tissue slices. In the theoretical simulation, we applied the Fresnel-Kirchhoff diffraction theory including possible optical aberrations to compute the images at 0.8 and 1.2 THz. It was found that the experimental data are highly consistent with the simulations, indicating that the observed artifacts can be well explained by the optical diffraction that was caused by the edge of the sample. This work is instructive for THz imaging and can help correctly interpret the images obtained with the THz-TDS imaging technique.

## 2. Experiment and theoretical analysis

### 2.1. Experiment section

#### 2.1.1. Sample preparation

Approval for the animal experiments involved in this study was granted by the Institutional Animal Care and Use Committee, Chongqing Institute of Green and Intelligent Technology, Chinese Academy of Sciences. To obtain mouse melanoma tissue slices, the 7 weeks old BABL/C mice were sacrificed by cervical dislocation first, and then its fresh melanoma was taken out and pre-fixed with 4% paraformaldehyde solution at 4 °C for 24 hours. After fixation, the melanoma tissue was removed from the paraformaldehyde solution and transferred to a freezing microtome (CM3050S, Leica Biosystems Nussloch GmbH, Nussloch, Germany) for slicing. In our slicing program, the optimum cutting temperature compound (OCT, 10.24% polyvinyl alcohol, 4.26% polyethylene glycol and 85.5% nonreactive ingredients) (REF4583, Sakura Finetek USA, Inc., Torrance, USA) was used as an embedding medium to obtain the slices with a flat surface. The OCT embedded melanoma tissue was cut into slices with the thickness about 100  $\mu\text{m}$  following the traditional slicing procedure [6,7]. Each of the frozen slices was put in a hollow double-sided tape with a diameter of 15 mm and a thickness about 100  $\mu\text{m}$ , and then sandwiched between two polystyrene slides that have weak THz absorption (the absorption coefficient is about  $10\text{ cm}^{-1}$  at 1.2 THz). In this way, the tissue slices can be measured by the THz-TDS system in transmission mode and the dehydration of the sample can be effectively prevented.

To explore the underlying mechanism of the artifact in THz imaging, a commercial vinyl coverslip with a thickness of 240  $\mu\text{m}$  (22 mm  $\times$  22 mm, Fisherbrand, UK) was used as the standard sample. The coverslip was thoroughly cleaned before the THz measurement by washing with water and ethanol alternately for three times to eliminate possible contaminated particles on the coverslip that may cause THz scattering.

#### 2.1.2. Setup for THz-TDS

A THz-TDS system (T-ray 5000, Advanced Photonix Inc., New York, USA) with a dynamic range about 76 dB @ 0.28 THz and a spectral resolution of 3.13 GHz was employed to inspect the sample in a clean room maintained at a temperature of  $22 \pm 0.5\text{ }^{\circ}\text{C}$  and a relative humidity of  $50 \pm 2\%$  [15]. In this system (Fig. 1(a)), the THz radiation emitted from a photoconductive antenna (1) was pre-collimated by a high-resistance hyper hemisphere Si lens (2), and then focused to a spot (e.g., with a radius about 0.625 mm@1.2 THz) by a high-density polyethylene plano convex lens (3) with a diameter of 38.1 mm and a focal length of 152.4 mm. The THz radiation, transmitted

through the sample (4), was refocused by a similar high-density polyethylene plano convex lens (5) and detected by another photoconductive antenna (7) coupled with a high-resistance hyper hemisphere Si lens (6). A typical time-domain spectrum and its corresponding frequency-domain spectrum of the system without samples is presented in Fig. 1(b) and 1(c), respectively.

### 2.1.3. THz imaging

In THz imaging, the sample was fixed in a sample holder and installed on a two-dimensional motorized precision translation stage with the sample surface coinciding with the focal plane of the THz beam [16]. To obtain a high signal-to-noise ratio while keep the imaging time short, a step size of 0.1 mm and a scan rate of 0.1 s for each pixel were adopted in the spectroscopy imaging process. The detected time-domain spectral signal for each pixel was transformed to the frequency-domain spectrum by the fast Fourier transform (FFT) algorithm [15,17], and the amplitude or intensity pseudo-color image was constructed at certain frequencies.

### 2.1.4. Determination of the THz beam waist diameter

The knife-edge method was employed to determine the THz beam waist diameter of the THz-TDS system at a certain frequency [18–20]. Briefly, a high-alloyed stainless steel microtome blade was firstly imaged by the THz-TDS system and the THz amplitude image was built at a desired frequency (e.g., 1.2 THz). Then, a line profile of the image was extracted (Fig. 1(d)) and its first derivative was obtained and fitted to a Gaussian function (Fig. 1(e)). Finally, the waist radius of the THz beam was obtained from the fitted peak by approximating the waist radius as the lateral distance between the peak center and the location where the signal decays to its 1/e. As shown in Fig. 1(e), the obtained THz beam waist radius is about 0.625 mm at 1.2 THz (corresponding to the wavelength of 0.25 mm), i.e., the THz beam waist diameter is 1.25 mm at this frequency. By analyzing the waist diameters at different frequencies (0.5–2.0 THz), we found that the waist diameter of the THz beam is about 5 folds of the THz wavelength for the investigated frequencies.

## 2.2. Theoretical analysis

To explain the phenomenon observed in our experiment, we carried out simulations based on the Fresnel-Kirchhoff diffraction theory by taking the THz beam as the Gaussian beam [21]. The Fresnel-Kirchhoff diffraction formula is given by:

$$\tilde{E}(\vec{r}, z) = \frac{e^{ikz}}{i\lambda z} \iint \tilde{E}(S)H(\omega) \exp\left[\frac{ik(\vec{r} - \vec{r}')^2}{2z}\right] dx' dy' \quad (1)$$

where  $\lambda$  is the wavelength of incident light,  $k = 2\pi/\lambda$  is the wavenumber,  $\tilde{E}(s)$  denotes the electric field distribution at the front surface of the sample,  $z$  is the distance between the back surface of the sample and the front surface of the high-density polyethylene plano convex lens (5),  $H(\omega)$  is the complex transfer function introduced to describe the modulation of the THz electric field by the sample,  $\vec{r} = (x, y)$  and  $\vec{r}' = (x', y')$  are the transverse radial vectors, respectively.

A Gaussian function is used to describe the incident beam  $\tilde{E}(s)$ , written as:

$$\tilde{E}(S) = \frac{E_0 F}{i(z_1 - iF)} \exp\left(ikz_1 + \frac{ik\vec{r}'^2}{2(z_1 - iF)}\right) \quad (2)$$

where  $E_0$  is the amplitude of the electric field,  $F = \pi D^2/\lambda$  is the confocal parameter of the beam and  $D$  is the diameter of the beam's waist,  $z_1$  is the distance between the focal plane and the front surface of the sample.

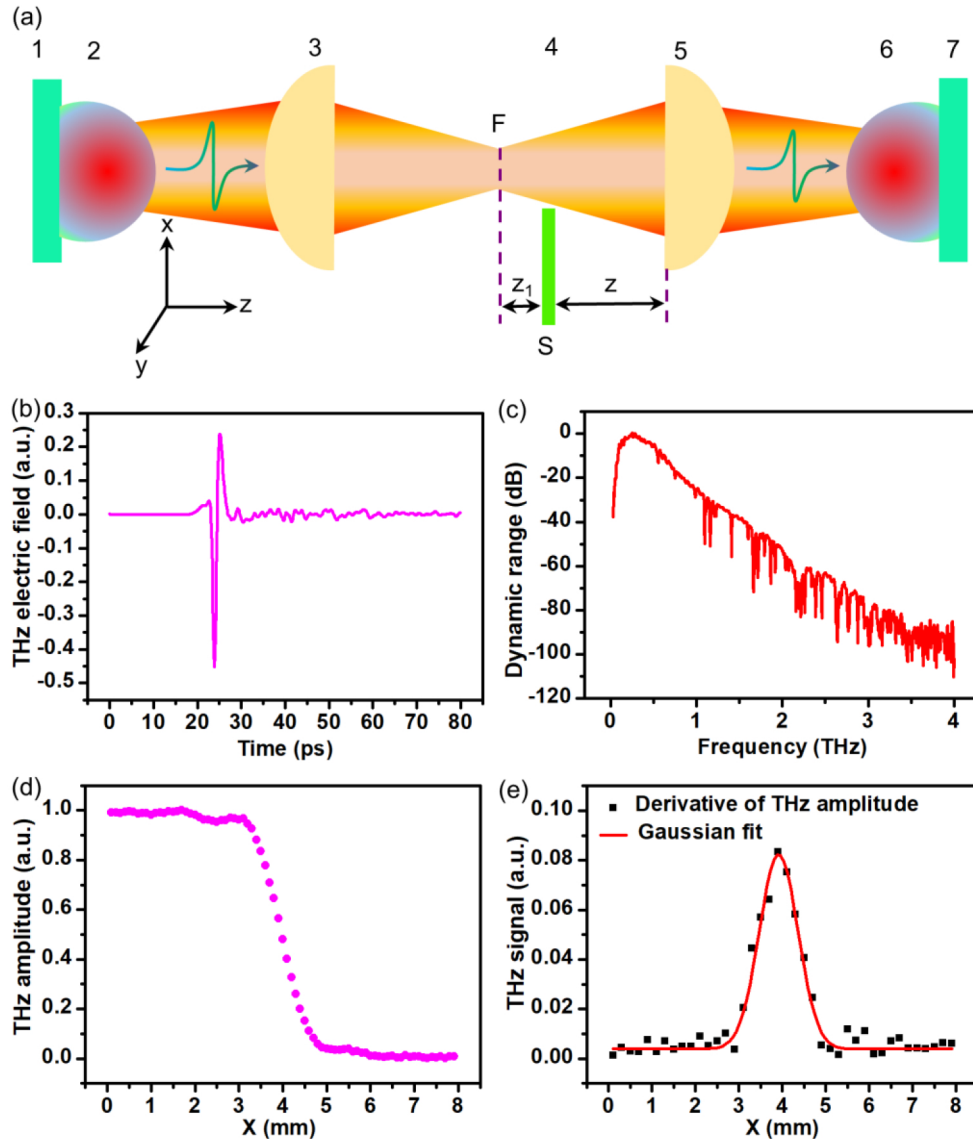


**Fig. 1.** The THz-TDS system and the determination of the radius of the THz beam by the knife-edge method. (a) Schematic of the THz path of the THz-TDS system. (1) and (7) Photoconductive antennae; (2) and (6) High-resistance hyper hemisphere Si lenses; (3) and (5) High-density polyethylene plano convex lenses; (4) Sample. The sample was positioned in the optical path with the aid of a miniature optical clamping device installed on a two-dimensional motorized precision translation stage. A laser level was used in the installation of the sample to ensure that the sample was perpendicular to the incident direction of the terahertz beam. The focus plane is indicated by a dashed line accompanied with the character 'F'; the green bar with the character 'S' indicates the sample position in the Z axis. ' $z_1$ ' indicates the distance between the front surface of the sample and the focus plane, namely, the defocus distance. (b) A typical time-domain spectrum and (c) the corresponding frequency-domain spectrum of the system free of samples. (d) The line profile extracted from the THz amplitude image at 1.2 THz. (e) The first derivative (black square dot) of the THz amplitude data in (d), fitted by a Gaussian function (red curve).

Supposing the sample edge is sharp enough, which is infinite along the  $x$  and  $y$  axis, the transfer function  $H(\omega)$  of the sample can be written as:

$$H(\omega) = \begin{cases} \exp\left(i\frac{(n-1)\omega h}{c}\right) \cdot \exp(-\alpha h) & 0 \leq x \leq d, 0 \leq y \leq l \\ 1 & x < 0, x > d, y < 0, y > l \end{cases} \quad (3)$$

where  $n$  and  $\alpha$  are the refractive index and absorption coefficient of the sample,  $\omega$  is the angular frequency of THz wave,  $h$  is the thickness of the sample in the normal incidence, and  $c$  is the speed of light in vacuum.  $d$  and  $l$  are the width and length of the phase step, respectively. Here, we define the air-sample edge is the zero point of  $x$  and  $y$ , and the sample-air edge locates at  $x = d$  and  $y = l$ , respectively. Obviously, the value of  $\tilde{E}(\vec{r}, z)$  will depend on the location of the focal spot, since the spot keeps moving along  $x$  and  $y$  axis and covers different area of the sample each time.

Based on the Eqs. (1–3), the relation between  $\tilde{E}(\vec{r}, z)$  and  $x$  and  $y$  can be computed, which can be used for the comparison with the experimental results.

### 2.3. Results and discussion

#### 2.3.1. THz images of the melanoma tissue slice and vinyl coverslip

A typical THz intensity image of the melanoma tissue slice is shown in Fig. 2(a). In the image, the edge of the tissue slice is in an irregular shape with a red color. The red color in the image indicates a lower THz power while the yellow color means a higher THz power. It can be seen from the image that more power loss occurred at the edge of the sample. Surprisingly, it was observed a pattern in the image that seems like a scaled down contour of the tissue edge. Similar phenomenon was also observed in the THz image of commercial vinyl coverslip (Fig. 2(b)).

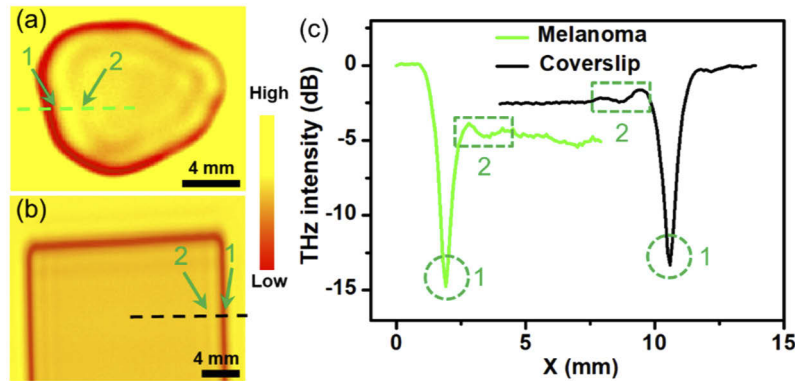


**Fig. 2.** Artifacts observed in the THz intensity images of two different samples at 1.2 THz. (a) THz intensity image of a melanoma tissue slice, (b) THz image of a vinyl coverslip, (c) Section profiles along the dashed lines shown in (a) and (b). In THz images, the locations corresponding to the edge and inside pattern are marked by ‘1’ and ‘2’, respectively. In the section profiles, the locations corresponding to the edge and inside pattern are marked by dashed circles and rectangles, accompanied with ‘1’ and ‘2’, respectively.

To evaluate this phenomenon in-depth, we further analyzed the THz intensity of the images. An example is shown in Fig. 2(c), from which we can observe the intensity change along the dashed lines quantitatively. Obviously, the THz power losses are significant at the edges (marked by ‘1’) of the samples while the losses are very moderate (marked by ‘2’) at where the patterns appeared. At first thought, one may ascribe the phenomenon occurred at the edge to the scattering



effect. However, the scattering of the sample edge cannot result in such a high power loss by considering that the THz wave is incident perpendicularly on the sample and that the surface roughness around the sample edge is much smaller than the THz wavelength. To the best of our knowledge, there is also no direct information available on the origin of the patterns observed inside both samples.

### 2.3.2. Artifacts in the THz image of vinyl coverslip

To explore the underlying mechanisms of the phenomena observed above, we initiated a detailed study on the standard vinyl coverslip by considering the section profiles covering the full width at different frequencies from 0.5 to 2.0 THz. We chose this frequency range for in-depth analysis by considering: (1) for the frequency lower than 0.5 THz the quality of THz images is poor due to the large diameter of the THz beam, and (2) for the frequency higher than 2.0 THz the quality of the THz image is also poor due to the small dynamic range of the signal. This range is wide enough to demonstrate the artificial phenomenon. As an example, the THz intensity image of the coverslip at 0.8 THz with full width is shown in Fig. 3(a), in which the left and right edges (marked by '1' and '4', respectively) and the corresponding edges (marked by '2' and '3', respectively) of the inside pattern were observed having different contrasts. This is manifested in Fig. 3(b) that shows the section profiles of the THz intensity images of the coverslip along the green line in Fig. 3(a). It is evident from Fig. 3(b) that the profiles of the THz intensity at 0.8 and 1.2 THz have different features. This is quite understandable because the response of a dielectric material to THz radiation is frequency dependent. The refractive index and the absorption coefficient of the vinyl coverslip are both frequency dependent. For any of the two frequencies, the profile shows two noticeable different valleys around the left and right sample edges (marked by the dashed circles 1 and 4, respectively) and observable different signals of the left and right sides of the inside pattern (marked by the dashed rectangles 2 and 3, respectively).

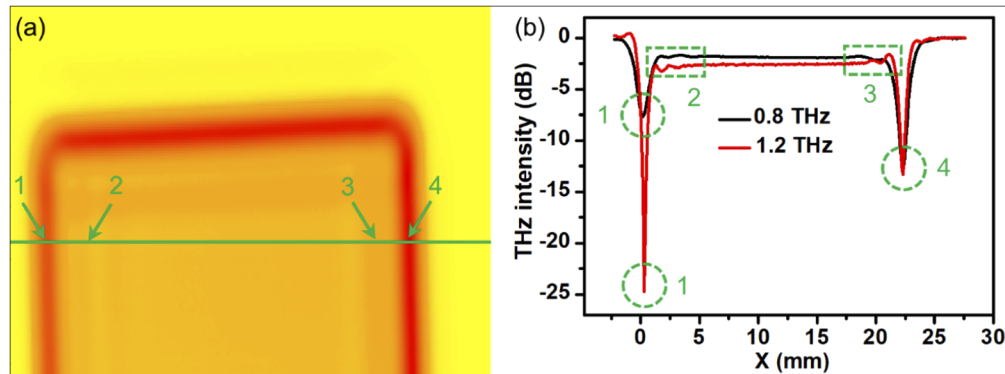


**Fig. 3.** An in-depth examination of the THz intensity image of the vinyl coverslip. (a) THz intensity image of the coverslip at 0.8 THz, and (b) the section profiles (along the green line in (a)) of the THz intensity images at 0.8 and 1.2 THz, respectively. '1' and '4' indicate the left and right edges of the sample, respectively; and '2' and '3' indicate the left and right edges of the inside pattern, respectively. The dashed circles and rectangles are used to mark the signals at the corresponding locations, accompanied with '1', '2', '3' and '4'.

It is worthwhile to note that the quality of the THz beam was checked by using an iris diaphragm in our experiments. We have put an iris diaphragm close to the left-side surface of the sample (Fig. 1(a)), and imaged the sample under various diaphragm opening diameters (1 mm, 3 mm, 5 mm, and 10 mm) or without the diaphragm. The observed artificial phenomena (Fig. 4) were highly consistent, regardless of the opening diameters. The observations indicate that the

quality of the THz beam in our system is good enough, and the diffraction of the beam itself has negligible contribution to the artificial images observed above.

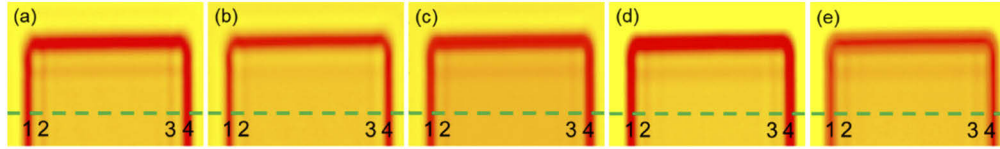


**Fig. 4.** THz images of a vinyl coverslip at 0.8 THz with different diaphragm opening diameters. (a) 1 mm; (b) 3 mm; (c) 5 mm; (d) 10 mm; and (e) without the diaphragm. '1' and '4' indicate the left and right edges of the sample, respectively; and '2' and '3' indicate the left and right edges of the inside pattern, respectively.

### 2.3.3. Mechanisms of artifacts

According to current available knowledge, the Fresnel-Kirchhoff diffraction theory (see the section 2.2 *Theoretical analysis*) was resorted to interpret the underlying mechanisms of the observed phenomena. To do this, the refractive index and the absorption coefficient of vinyl coverslip are firstly calculated from the obtained THz-TDS data [7], which are plotted against the frequency (Fig. 5(a)). Afterwards, the Eqs. (1–3) were applied to compute the THz intensity of the coverslip by taking the THz beam as a Gaussian beam with a diffraction distance of 152.4 mm and a frequency-dependent beam diameter determined according to the knife-edge method detailed in the section 2.1.4 *Determination of the THz beam waist diameter*. As an example, the simulated THz intensity profiles across the coverslip at 0.8, 1.2 and 1.5 THz are shown in Fig. 5(b). Indeed, high power losses at the edges (marked by the dashed circles indicated by '1' and '4', respectively) of the coverslip were observed and the inside pattern (marked by the dashed rectangles '2' and '3', respectively) was also appeared at the expected location. The artificial phenomenon is nonlinearly dependent on the frequency and governed by the Eq. (3). As shown in this example, the artificial phenomenon occurred at 1.2 THz was the most prominent one, rather than the one occurred at 1.5 THz.

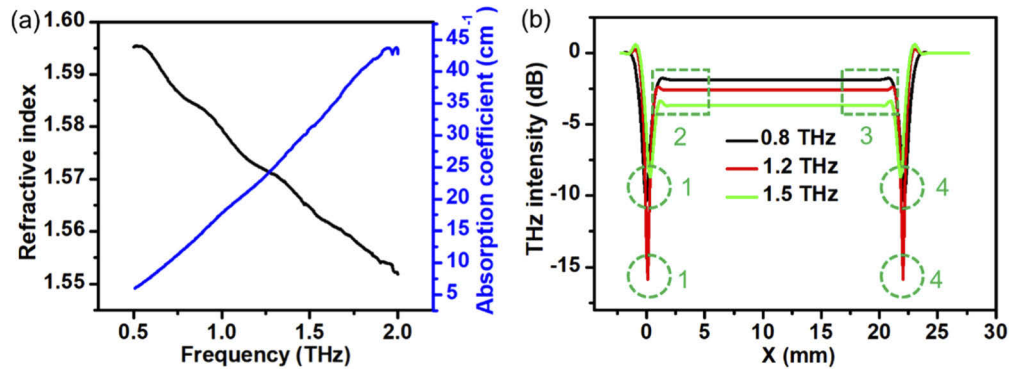


**Fig. 5.** Simulation of the artifacts with the Fresnel-Kirchhoff diffraction theory. (a) The refractive index and absorption coefficient of vinyl coverslip plotted against the frequency region of 0.5–2.0 THz. (b) Simulated THz intensity profiles across the coverslip at 0.8, 1.2 and 1.5 THz. '1' and '4' indicate the left and right edges of the sample, respectively; and '2' and '3' indicate the left and right edges of the inside pattern, respectively.

It was noticed that there are some differences between the simulated results and the experimentally observed results (Fig. 3(b)). For example, the simulated power loss at the left edge of

the coverslip is the same as that of the right edge at a certain frequency (e.g., 0.8 THz), but the experimentally observed power losses at the two different edges are very different. Furthermore, the simulated power losses at the left and right sides of the inside pattern are also the same, but those observed experimentally are different. These results indicate that other factors need to be carefully considered to accurately interpret the experimentally observed phenomena. In practice, optical aberrations often exist in a THz-TDS system to some degree [22,23]. Unfortunately, it is difficult to perfectly align the optical components and exactly focus the beam on the sample due to that THz wave is invisible to naked eyes. For examples, it is challenging to align the THz emitter and the detector on the same line, and the THz beam may be de-focused, for instance it can be focused in front of the sample surface. In addition, the focal plane is frequency-dependent, so THz waves at different frequencies will be focused on different planes when the whole THz-TDS setup is fixed. To properly interpret the observed artifacts, these factors should be considered. As it is infeasible to accurately measure these parameters for an already well-aligned THz-TDS system, we tested a series of possible parameters in the simulation when using the Fresnel-Kirchhoff diffraction theory. As demonstrated in Fig. 6, the simulated results can well match the experimental data when the detector is assumed left-positioned 2.6 mm off the optical axis of the THz beam emitted from the emitter while the beam defocusing obeys an empirical equation  $Z_1 = 3.85f + 0.225$  in the range from 0.5 to 2.0 THz. In the equation,  $Z_1$  is the defocused distance (mm) and  $f$  is the frequency (THz). It can be easily calculated that the defocused distances are 3.305 mm and 4.845 mm for 0.8 THz and 1.2 THz, respectively. For now, we can confirm that the artifacts observed in THz-TDS imaging can be properly interpreted by the Fresnel-Kirchhoff diffraction theory in which the misalignment of the detector and the beam defocus are included.

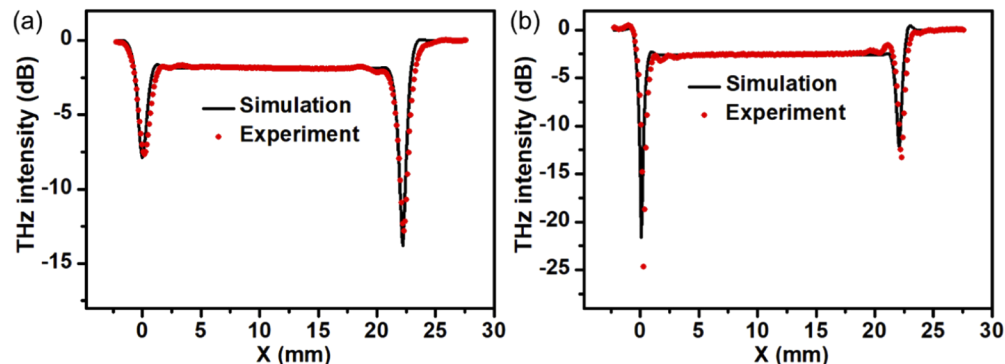


**Fig. 6.** Comparison between the simulated results and the experimental data for different frequencies. (a) 0.8 THz, and (b) 1.2 THz. In the simulation, the optical aberrations are considered, including off-axis optical detector alignment and THz beam defocus.

### 3. Conclusion

An artifact was observed in the THz images of biological melanoma tissue slices investigated by a THz-TDS system. It was found from the THz intensity image that a higher power loss occurred at the sample edge and a pattern similar to the edge contour appeared inside the image. By taking a vinyl coverslip as the standard sample for an in-depth study, it can be concluded that only the Fresnel-Kirchhoff diffraction theory alone cannot be used to well interpret the observed phenomenon. However, the theory can be well applied to interpret the experimental results when optical aberrations in the THz-TDS system, including the detector's off-axis alignment and the THz beam defocusing, were introduced in the theoretical simulation. The current work sheds



lights into interpreting THz-TDS images, which is helpful for proper and wide application of the THz-TDS imaging technique, particularly for its implementation in biological studies.

**Funding.** Natural Science Foundation of Chongqing (cstc2018jcyjAX0405, cstc2019jcyj-msxmX0051); National Natural Science Foundation of China (61875092, U1932132); The University of Chinese Academy of Sciences Supported Program for Tackling Key Problems in Science and Technology (E029610601); National Key Research and Development Program of China (2017YFF0106303).

**Disclosures.** The authors declare that there are no conflicts of interest related to this manuscript.

**Data availability.** Data underlying the results presented in this paper are not publicly available at this time but may be obtained from the authors upon reasonable request.

## References

1. J. D. Buron, D. H. Petersen, P. Boggild, D. G. Cooke, M. Hilke, J. Sun, E. Whiteway, P. F. Nielsen, O. Hansen, A. Yurgens, and P. U. Jepsen, "Graphene conductance uniformity mapping," *Nano Lett.* **12**(10), 5074–5081 (2012).
2. B. Ferguson and X. C. Zhang, "Materials for terahertz science and technology," *Nat. Mater.* **1**(1), 26–33 (2002).
3. X. Yang, X. Zhao, K. Yang, Y. P. Liu, Y. Liu, W. L. Fu, and Y. Luo, "Biomedical applications of terahertz spectroscopy and imaging," *Trends Biotechnol.* **34**(10), 810–824 (2016).
4. Z. J. Zhu, J. B. Zhang, Y. S. Song, C. Chang, G. H. Ren, J. X. Shen, Z. C. Zhang, T. Ji, M. Chen, and H. W. Zhao, "Broadband terahertz signatures and vibrations of dopamine," *Analyst* **145**(18), 6006–6013 (2020).
5. Z. B. Yang, D. Y. Tang, J. Hu, M. J. Tang, M. K. Zhang, H. -L. Cui, L. H. Wang, C. Chang, C. H. Fan, J. Li, and H. B. Wang, "Near-field nanoscopic terahertz imaging of single proteins," *Small* **17**(3), 2005814 (2021).
6. G. S. Geng, G. B. Dai, D. D. Li, S. L. Zhou, Z. X. Li, Z. B. Yang, Y. H. Xu, J. G. Han, T. Y. Chang, H. -L. Cui, and H. B. Wang, "Imaging brain tissue slices with terahertz near-field microscopy," *Biotechnol. Prog.* **35**(2), e2741 (2019).
7. D. D. Li, Z. B. Yang, A. L. Fu, T. N. Chen, L. G. Chen, M. J. Tang, H. Zhang, N. Mu, S. Wang, G. Z. Liang, and H. B. Wang, "Detecting melanoma with a terahertz spectroscopy imaging technique," *Spectrochim. Acta, Part A* **234**, 118229 (2020).
8. K. I. Zaitsev, N. V. Chernomyrdin, K. G. Kudrin, I. V. Reshetov, and S. O. Yurchenko, "Terahertz spectroscopy of pigmentary skin nevi in vivo," *Opt. Spectrosc.* **119**(3), 404–410 (2015).
9. J. Shi, Y. Y. Wang, T. N. Chen, D. G. Xu, H. L. Zhao, L. Y. Chen, C. Yan, L. H. Tang, Y. X. He, H. Feng, and J. Q. Yao, "Automatic evaluation of traumatic brain injury based on terahertz imaging with machine learning," *Opt. Express* **26**(5), 6371–6381 (2018).
10. L. Y. Xing, H. -L. Cui, C. C. Shi, Z. Y. Zhang, J. Zhang, T. Y. Chang, D. S. Wei, C. L. Du, S. N. Zhang, and Z. X. Zhou, "Nondestructive examination of polymethacrylimide composite structures with terahertz time-domain spectroscopy," *Polym. Test.* **57**, 141–148 (2017).
11. X. Zhao, M. K. Zhang, D. S. Wei, Y. X. Wang, S. H. Yan, M. W. Liu, X. Yang, K. Yang, H. -L. Cui, and W. L. Fu, "Label-free sensing of the binding state of MUC1 peptide and anti-MUC1 aptamer solution in fluidic chip by terahertz spectroscopy," *Biomed. Opt. Express* **8**(10), 4427–4437 (2017).
12. Z. Y. Song, S. H. Yan, Z. Y. Zang, Y. Fu, D. S. Wei, H. -L. Cui, and P. X. Lai, "Temporal and spatial variability of water status in plant leaves by terahertz imaging," *IEEE Trans. Terahertz Sci. Technol.* **8**(5), 520–527 (2018).
13. S. Yamaguchi, Y. Fukushi, O. Kubota, T. Itsuji, T. Ouchi, and S. Yamamoto, "Brain tumor imaging of rat fresh tissue using terahertz spectroscopy," *Sci. Rep.* **6**(1), 30124 (2016).
14. D. M. Mittleman, "Twenty years of terahertz imaging invited," *Opt. Express* **26**(8), 9417–9431 (2018).
15. Z. B. Yang, S. L. Feng, W. Yao, J. G. Han, and H. B. Wang, "Synthesis of novel rambutan-like graphene@aluminum composite spheres and non-destructive terahertz characterization," *RSC Adv.* **9**(6), 3486–3492 (2019).
16. M. D. Hu, M. J. Tang, H. B. Wang, M. K. Zhang, S. P. Zhu, Z. B. Yang, S. L. Zhou, H. Zhang, J. Hu, Y. S. Guo, X. Wei, and Y. S. Liao, "Terahertz, infrared and Raman absorption spectra of tyrosine enantiomers and racemic compound," *Spectrochim. Acta, Part A* **254**, 119611 (2021).
17. X. Zhao, Z. Q. Lin, Y. X. Wang, X. Yang, K. Yang, Y. Zhang, J. Peng, M. L. de la Chapelle, L. Q. Zhang, and W. L. Fu, "Label-free self-referenced sensing of living cells by terahertz metamaterial-based reflection spectroscopy," *Biomed. Opt. Express* **10**(3), 1196–1206 (2019).
18. Y. X. Wang, Z. R. Zhao, Z. Q. Chen, L. Zhang, K. J. Kang, and J. K. Deng, "Continuous-wave terahertz phase imaging using a far-infrared laser interferometer," *Appl. Opt.* **50**(35), 6452–6460 (2011).
19. Y. X. Wang, Z. R. Zhao, Z. Q. Chen, L. Zhang, and K. J. Kang, "Diffraction-induced edge contrast enhancement for terahertz imaging," *Chin. Opt. Lett.* **7**(8), 690–693 (2009).
20. H. L. Zhao, Y. Y. Wang, L. Y. Chen, J. Shi, K. Ma, L. H. Tang, D. G. Xu, J. Q. Yao, H. Feng, and T. N. Chen, "High-sensitivity terahertz imaging of traumatic brain injury in a rat model," *J. Biomed. Opt.* **23**(3), 1 (2018).
21. M. Born and E. Wolf, *Principles of Optics*, 7<sup>th</sup> edition (Cambridge U. Press, 1999).
22. E. Abraham, H. Cahyadi, M. Brossard, J. Degret, E. Freysz, and T. Yasui, "Development of a wavefront sensor for terahertz pulses," *Opt. Express* **24**(5), 5203–5211 (2016).
23. M. Brossard, H. Cahyadi, M. Perrin, J. Degert, E. Freysz, T. Yasui, and E. Abraham, "Direct wavefront measurement of terahertz pulses using two-dimensional electro-optic imaging," *IEEE Trans. Terahertz Sci. Technol.* **7**(6), 741–746 (2017).